

Cite this: *J. Mater. Chem.*, 2011, **21**, 6698

www.rsc.org/materials

PAPER

# Mesoporous silica–metal organic composite: synthesis, characterization, and ammonia adsorption

Amanda M. B. Furtado, Jian Liu, Yu Wang and M. Douglas LeVan\*

Received 28th January 2011, Accepted 8th March 2011

DOI: 10.1039/c1jm10451a

A novel composite adsorbent composed of an inorganic silica phase impregnated with a metal organic phase is synthesized and characterized. Specifically, MCM-41 is impregnated with copper active sites, which are then functionalized with benzene-1,3,5-tricarboxylic acid, which is the linker in the metal organic framework CuBTC. X-ray diffraction, nitrogen adsorption isotherms, thermogravimetric analysis, scanning electron microscopy, X-ray photoelectron spectroscopy, and equilibrium ammonia capacities are used to characterize the composite and control materials. Properties of the composite and control samples after conditioning at 85 °C in saturated water vapor for 5 h are also evaluated. Results show that the silica phase of the composite material provides an engineered phase that enhances the hydrothermal stability of the metal organic phase and the metal organic phase provides active sites for chemisorption. The composite material has a high ammonia capacity of 5.2 mol kg<sup>-1</sup> and remains stable after conditioning. In comparison, the CuBTC structure degrades and shows low ammonia capacity after conditioning.

## 1 Introduction

Air purification is an integral technology in today's society. With the advent of air quality concerns ranging from pollution to terrorism, the ability to remove light gases such as toxic industrial chemicals from air or other gases is a necessity. In order to have high capacities for contaminant removal, adsorbent materials with high surface areas and small pore sizes are preferred. The introduction of metal active sites into adsorbent materials for chemisorption is also desired for air purification using single pass filters.<sup>1–8</sup>

Research into next generation adsorbent materials is ongoing. Some of the top candidates in this field among new materials are metal organic frameworks (MOFs), which exhibit large surface areas and open structures and can have high capacities for light gases.<sup>9</sup> MOFs consist of metal ions coordinated with organic linkers to form porous materials with extremely high surface areas and low densities.<sup>10</sup> The surface areas and pore sizes of these materials vary based on the size and type of the organic linkers, which are coordinated to metal oxide clusters to provide inorganic reactive sites that enhance the chemisorptive ability of the materials.<sup>11</sup> Variation in the type of metal oxide clusters allows these adsorbent materials to be designed for removal of targeted gases.

One major hurdle to wide-spread utilization of MOFs is their poor hydrothermal stability. The structure and porosity of some MOFs collapse upon exposure to water and high temperatures, thereby reducing their effectiveness for many air purification applications.<sup>12,13</sup> One such MOF, CuBTC, has unsaturated metal centers in its crystal structure, and water molecules have been found to bond quite strongly to these.<sup>14</sup> Kusgens *et al.*<sup>15</sup> reported that CuBTC can adsorb 35 mol kg<sup>-1</sup> water and not all of the molecules can be desorbed because of the chemisorption of free water on the unsaturated metal centers. According to the steam stability map generated by Low *et al.*,<sup>12</sup> CuBTC is a MOF that exhibits moderate hydrothermal stability. Liu *et al.*<sup>13</sup> reported that CuBTC is prone to lose carbon dioxide capacity after repeated water/carbon dioxide mixture isotherm measurements. In order for adsorption processes to be used with variable gas stream conditions in purification applications, adsorbents with better hydrothermal stabilities and high gas capacities are desirable.

Ordered mesoporous silicate (OMS) materials are a family of siliceous materials that are popular adsorbents due to their large surface areas and ordered porous structures. OMSs are formed *via* a liquid crystal templating mechanism using ionic surfactants as structure directing agents.<sup>16</sup> The mesoporous materials can be synthesized by condensing silica onto surfactant liquid crystals and then removing the surfactant from the final product.<sup>17</sup> These silica materials tend to have high adsorption capacities for some basic gases, such as ammonia,<sup>18–20</sup> and extensive modifications of OMS materials have been performed to enhance their adsorptive ability for other light gases. OMS materials are often used as structure directing agents to form carbonaceous materials with

Department of Chemical and Biomolecular Engineering, Vanderbilt University, PMB 351604, 2301 Vanderbilt Place, Nashville, TN, 37235-1604, USA. E-mail: m.douglas.levan@vanderbilt.edu; Fax: +(615) 343-7951; Tel: +(615) 322-2441

smaller pore sizes. They also can be used as the base material for composite materials.<sup>21</sup> Some OMS materials, such as highly ordered MCM-41, have been found to be stable at high temperature and relative humidities.<sup>23,24</sup>

Research on metal organic-containing composites has focused on incorporating carbonaceous materials into the composites. Petit and Bandoz<sup>25–27</sup> have reported a composite material made of MOF-5 and graphite oxide. It showed improvement in ammonia capacity in a dry environment when compared to a mixture of the two solids. However, the material was found to be unstable when tested at higher relative humidity. The group also reported a composite of CuBTC and graphite oxide which showed better hydrothermal stability.<sup>28</sup> Yang *et al.*<sup>29</sup> have reported the synthesis of a MOF-carbon nanotube composite. It was found to have higher surface area, enhanced thermal stability, and higher hydrogen storage capacity when compared to the base MOF material. Liu *et al.*<sup>30</sup> used MOF-5 as a template for a high surface area furfuryl alcohol-based carbonaceous material. After synthesis of the composite, the MOF was removed and the carbonaceous material was found to have an ultra-high surface area, on the order of 3000 m<sup>2</sup> g<sup>−1</sup>. Finally, Hundal *et al.*<sup>31</sup> successfully incorporated polyoxometalate anions into CuBTC and produced a thermally stable, microporous adsorbent material. Based on N<sub>2</sub> isotherm analysis, the composite material had a lower surface area than the initial CuBTC.

Ammonia is a toxic industrial chemical that has been widely studied for air filtration applications. According to guidelines set by the U. S. Occupational Safety and Health Administration,<sup>32</sup> ammonia is unsafe for human exposure above 35 ppm<sub>v</sub> for fifteen minutes or 25 ppm<sub>v</sub> for eight hours. Several studies have considered the adsorption of pure ammonia at equilibrium conditions. Helminen *et al.*<sup>33</sup> reported ammonia adsorption in traditional adsorbents, including activated carbon, alumina, polymer resin, silica gel, and several Type A and X zeolites. At room temperature and with pure ammonia at 1 atmosphere pressure, alumina, silica gel, and activated carbon have capacities ranging from 2.2 mol kg<sup>−1</sup> to 5.3 mol kg<sup>−1</sup>, while 13X zeolite and polymer resins have values of 9.0 mol kg<sup>−1</sup> and 11.3 mol kg<sup>−1</sup>, respectively. In a more recent study, Doonan *et al.*<sup>34</sup> showed that a covalent organic framework, COF-10, has a large equilibrium pure ammonia capacity at STP of approximately 15 mol kg<sup>−1</sup>. To gather information closer to adsorbent operating conditions, other studies have investigated ammonia capacities at lower ammonia concentrations and under dynamic conditions. Britt *et al.*<sup>11</sup> studied harmful gas adsorption in different MOFs and obtained a dynamic ammonia capacity of 5.1 mol kg<sup>−1</sup> for CuBTC with 1% NH<sub>3</sub> in a mixed gas. Petit *et al.*<sup>28</sup> reported a dynamic ammonia capacity of 8.8 mol kg<sup>−1</sup> for a CuBTC–graphene composite using 1000 ppm NH<sub>3</sub> in dry air. For air filtration applications, the concentration of ammonia in product air is generally in the parts per million range and closer to the testing conditions of Britt *et al.* and Petit *et al.* rather than those reported using pure ammonia. Because this research focuses on air filtration, the following study includes the measurement of ammonia equilibrium capacities at a reduced ammonia concentration (1500 ppm<sub>v</sub>), which is orders of magnitude more dilute than pure ammonia, and generally yields lower ammonia capacity values for common adsorbents.

To date, there have been no published accounts of composite materials composed of an ordered mesoporous silica phase modified with a metal organic molecule. This paper reports the synthesis and characterization of an ordered mesoporous silica–metal organic (MSMO) composite material that has a high capacity for ammonia adsorption and enhanced hydrothermal stability over the metal organic framework alone. The silica phase of the composite material provides an engineered phase to enhance the hydrothermal stability of the composite, and the metal organic phase provides active sites for chemisorption. Characterization methods for the composite include N<sub>2</sub> adsorption isotherms, X-ray diffraction, X-ray photoelectron spectroscopy, thermogravimetric analysis, and scanning electron microscopy.

## 2 Experimental methods

### 2.1 Materials

Tetramethylammonium hydroxide pentahydrate, (TMAOH, 97%), tetramethylammonium silicate solution, (TMA Si, 99.99%, 15–20 wt % in water), sulfuric acid (95.0–98.0%), and toluene (99%) were purchased from Sigma Aldrich. Hexadecyltrimethylammonium chloride (CTAC, 25% in water) was purchased from Pfaltz and Bauer. A solution of ammonium hydroxide (29 wt % in water), fumed silica (Cab-O-Sil M5), and ACS grade copper nitrate were purchased from Fisher Scientific. Benzene-1,3,5-tricarboxylic acid (BTC) and ACS grade ethanol were purchased from Acros Organics.

### 2.2 MCM-41 synthesis

MCM-41 with a 37 Å pore was synthesized based on the procedure outlined by Glover *et al.*<sup>21</sup> The reaction gel was formed by mixing a solution of 2.4 g of 29 wt % ammonium hydroxide and 21.2 g of 29 wt % CTAC with a solution of 3.04 g of TMAOH and 20 g of 10 wt % solution of TMA Si and then adding 4.5 g of Cab-O-Sil M5 fumed silica to the solution. After stirring for 30 min, the reaction gel was placed in a Teflon-lined autoclave and held at 80 °C in an oven for four days. Every 24 h, the autoclave was removed from the oven and titrated to a pH of 10.0 using concentrated sulfuric acid, for a total of three titrations. At 24 h after the third titration, the product was filtered and washed with distilled water to remove the remaining surfactant and allowed to dry at room temperature for 48 h. The calcination procedure used to burn the surfactant from the MCM-41 involved heating the as-synthesized MCM-41 in air from room temperature to 540 °C at a rate of 1 °C min<sup>−1</sup> and holding the sample at 540 °C for 10 h.

### 2.3 Composite synthesis

To produce the copper nitrate-impregnated MCM-41 sample, 0.5 g MCM-41 and 0.16 g copper nitrate (corresponding to one Cu atom per 9 Si atoms) were stirred in an aqueous solution for 3 h. After stirring, the sample (10 mol % Cu-MCM-41) was dried at 80 °C until dry. The sample was then heated in a tube furnace following the temperature schedule of the MCM-41 calcination procedure.

To incorporate the MOF phase, 0.21 g (1.0 mmol) of benzene-1,3,5-tricarboxylic acid was reacted with 0.1 g of copper-impregnated MCM-41 in a 60 ml mixed solution composed of equal parts by volume of water and ethanol. The mixture was placed in a Teflon-lined autoclave, and the reaction was held at 120 °C for 12 h. Light green crystals were collected after decanting the mother liquid and filtering the remaining mixture. The as-synthesized composite material was first dried in air and then placed in an oven at 120 °C overnight to obtain the final purple composite material. This same procedure was followed to synthesize a control sample, in which BTC was impregnated on base MCM-41 without copper impregnation.

## 2.4 Materials characterization

**2.4.1 Textural characterization.** Adsorption isotherms were measured at −196.1 °C using a Micromeritics ASAP 2020 with ultra high purity nitrogen as the analysis gas. Prior to measurement, approximately 0.1 g of each sample was degassed for 8 h with heating to 120 °C and vacuum to 10 μbar.

**2.4.2 X-ray diffraction (XRD).** XRD spectra were used to confirm the long range structure of the MCM-41 and to confirm that the metal-impregnated samples also maintained the native MCM-41 structure. In addition, XRD was used to study the change of crystal structure before and after the samples were conditioned. The spectra were measured using a Scintag X1h/h automated powder diffractometer with Cu target, a Peltier-cooled solid-state detector, a zero background Si(5 1 0) support, and with a copper X-ray tube as the radiation source.

**2.4.3 Thermogravimetric analysis (TGA).** TGA was used to determine the amount of organic phase impregnated within the MCM-41 material. The material was heated in a stream of zero air flowing at 10 mL min<sup>−1</sup> at a ramp rate of 5 °C per minute to 700 °C and held at 700 °C for 2.5 h.

**2.4.4 Scanning electron microscopy (SEM).** SEM was used to visualize the microscopic properties of the materials. The images were collected using a Hitachi S4200 high resolution SEM equipped with a cold field emission electron gun, digital imaging, and a thin-window energy dispersive X-ray spectrometer (EDS). Spectra were collected at 2 kV.

**2.4.5 X-ray photoelectron spectroscopy.** XPS was performed with a PHI Versaprobe XPS Microprobe analysis system manufactured by Physical Electronics, Inc. The apparatus was equipped with a monochromatic Al K $\alpha$  X-ray source ( $E = 1486.6$  eV). Spectra were collected over binding energies ranging from 1300 to 100 eV, with high resolution carbon spectra collected over binding energies ranging from 298 to 280 eV, and high resolution copper spectra collected between 957 and 927 eV. The pass energy was set to 23.5 eV for determination of atomic ratios, and binding energies were referenced to the oxygen 1s peak.<sup>35</sup> All samples were analyzed after being crushed to a fine powder to expose the inner surface of MCM-41.

**2.4.6 Hydrothermal conditioning.** Hydrothermal stability for gas phase adsorbents is the simultaneous resistance to

degradation at high temperatures and humidities. Various methods have been reported in the literature to study this property. The materials are often heated to a specified temperature while simultaneously passing steam over the sample.<sup>12,22</sup> Another accepted procedure is to place the sample in boiling water for a specified time period.<sup>36,37</sup> MOFs and other adsorbents are often tested for stability using the former technique, which allows for analysis of the crystallinity and porosity of the sample before its structure has fully degraded. In this way, it is possible to compare the hydrothermal stabilities of different materials under conditions that are just harsh enough to show differences in the samples without fully degrading the structure.

Samples were conditioned at high temperature and humidity using the first conditioning method to test their hydrothermal stability. A hot plate was used to heat an Erlenmeyer flask filled with 150 mL of water to boiling. The samples were placed on filter paper and suspended above the boiling water. The samples were held at 85 °C in saturated water vapor for 5 h to complete their conditioning. After conditioning, they were allowed to dry in air.

**2.4.7 Ammonia capacity measurement.** Equilibrium capacities for room temperature ammonia adsorption were measured for all samples using a breakthrough apparatus, a schematic of which is shown in Fig. 1. The concentration of ammonia in dry helium fed to the adsorbent bed was kept constant at 1133 mg m<sup>−3</sup> (1500 ppm<sub>v</sub>). Prior to analysis, all samples were regenerated under 10 μbar vacuum at 120 °C for 8 h. The capacity of the adsorbent material,  $n$  (mol ammonia kg<sup>−1</sup> adsorbent), was calculated from

$$n = \frac{F}{m} \int_0^\infty (c_0 - c) dt \quad (1)$$

where  $c_0$  is the feed concentration in units of mol m<sup>−3</sup>, and  $c$  is the effluent concentration at time  $t$ . The volumetric flow rate of gas through the adsorbent bed,  $F$ , was adjusted to yield a breakthrough time of approximately one hour. The mass of the sample,  $m$ , was approximately 10 mg and was contained in a small cylindrical adsorbent bed with an internal diameter of 4 mm.

Full breakthrough curves at low flow rates were measured using this apparatus, and the resulting capacities are equilibrium

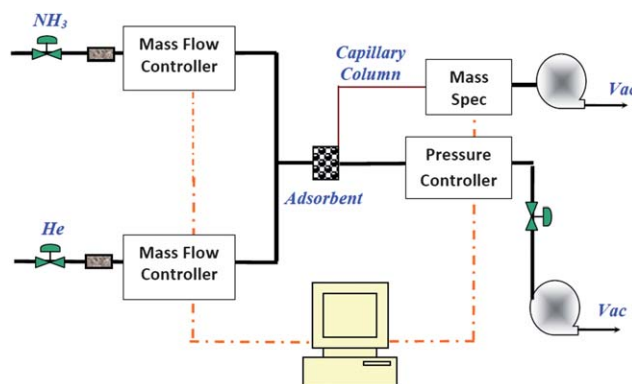


**Fig. 1** Schematic of the breakthrough apparatus used to determine ammonia capacities.

capacities. The accuracy of this method has been verified using a non-corrosive system. Capacities obtained by the full break-through method agree well with results obtained by standard gravimetric measurement using a Cahn balance.

### 3 Results and discussion

#### 3.1 Composite material characterization

Scanning electron microscope images, shown in Fig. 2, provide detailed information about the morphology of the composite material. The composite contains amorphous structures that are similar in appearance to the MCM-41 SEM images and do not possess large amounts of the octahedral crystals commonly seen for CuBTC. As discussed below for other analytical techniques, the SEM images are consistent with the formation of a composite material that has copper sites dispersed throughout the ordered MCM-41 phase with BTC molecules bound to these copper sites. BTC is not largely associated with a crystalline CuBTC phase formed in bulk; rather, the composite material consists of an ordered MCM-41 phase with BTC bound to copper sites dispersed throughout the silica matrix. Fig. 2(b) shows the presence of a crystalline impurity in the sample. As discussed below, only a small amount of this impurity is present, about 3 wt %, and it is CuBTC.

Fig. 3 depicts the nitrogen adsorption isotherm at  $-196.1\text{ }^{\circ}\text{C}$  for the impregnated material. The isotherm is Type IV based on the IUPAC classification scheme and is typical of a mesoporous MCM-41 material. Hysteresis due to capillary condensation in the mesopores is evident in the desorption branch of the isotherm. Based on the isotherm, the addition of copper active sites and BTC linkages throughout the MCM-41 does not decrease the mesoporosity of the material. A comparison of the composite with the MCM-41 sample indicates that the composite material is similar in mesoporosity to the base MCM-41. Table 1 summarizes the physical properties of the composite, the base MCM-41, and CuBTC. The addition of the BTC bound to the Cu active sites throughout the material yields a slight decrease in pore volume and increase in surface area when compared to the base MCM-41. When compared to CuBTC, the composite

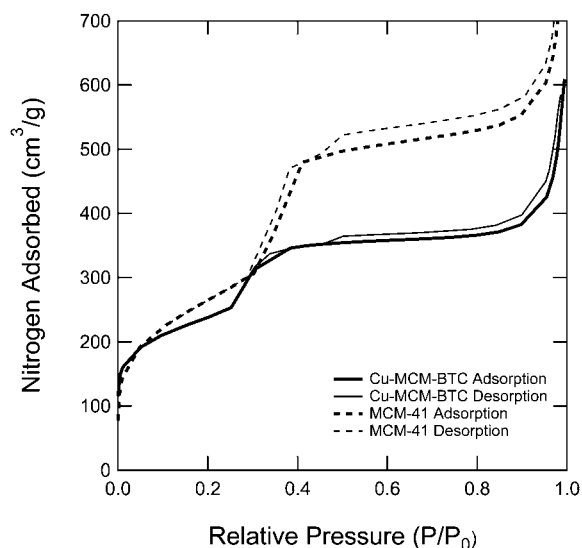


Fig. 3 Comparison of the MCM-41 and 10 mol % Cu-MCM-BTC composite nitrogen isotherms at 77 K.

material is 16% lower in surface area. The surface areas of the MCM-41 and the composite material are more similar than that of CuBTC and the composite, which is consistent with the BTC molecule attaching to the Cu active sites on the MCM-41 with minimal formation of crystalline CuBTC.

Fig. 4 summarizes the heating procedure and the weight loss of the composite material during heating using the TGA. The first step in the mass loss represents the removal of adsorbed water from the sample, and the second step represents loss of the organic BTC. Thermogravimetric analysis of the material shows a 12% loading of the organic BTC within the sample. No copper or silica is lost during this heating step because the vapor pressures of these substances are low.<sup>38</sup> The base MCM-41 was impregnated with copper nitrate at a ratio of 1 Cu atom to 9 Si atoms. With the MCM-41 considered to be  $\text{SiO}_2$ , this translates to 7.6 wt % copper being distributed throughout the silica matrix. This corresponds to a 2 : 1 Cu to BTC ratio, which is different from that of the CuBTC MOF, which has a 3 : 2 Cu to BTC ratio. Thus BTC binds to copper sites distributed throughout the silica matrix and does not form large quantities of crystalline CuBTC.

TGA was also performed on a control sample synthesized using BTC and MCM-41 without impregnated copper sites. This material was synthesized to determine if copper active sites are necessary to retain the BTC by bonding with the carboxylic acid groups on the organic molecule. TGA of this control sample showed only water loss and no removal of BTC from the sample,

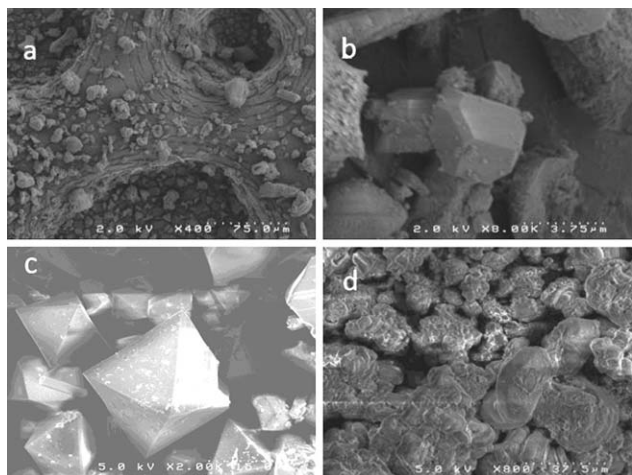
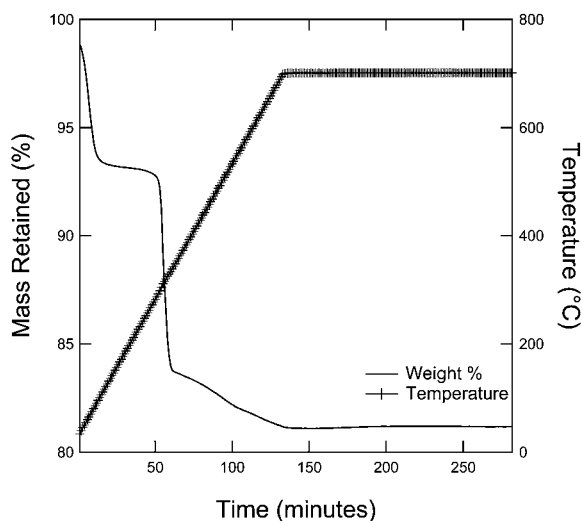


Fig. 2 SEM images of (a) Cu-MCM-BTC, (b) CuBTC impurity in Cu-MCM-BTC, (c) CuBTC, and (d) MCM-41.

Table 1 BET surface areas and pore volumes of MCM-41, CuBTC, and Cu-MCM-BTC

Sample	BET Surface Area ( $\text{m}^2\text{ g}^{-1}$ )	Total Pore Volume ( $\text{cm}^3\text{ g}^{-1}$ )
CuBTC	1004	0.49
MCM-41	809	1.09
Cu-MCM-BTC	836	0.94





**Fig. 4** TGA heating procedure and mass loss of the Cu-MCM-BTC composite.

indicating that no BTC remained on the silica support after synthesis. Thus, it is evident that copper sites distributed throughout the MCM-41 matrix are necessary to retain the BTC in the composite because they bond with oxygen atoms available on BTC. Because the composite material has well dispersed copper sites and does not form large amounts of crystalline CuBTC, not all carboxylic acid groups on each BTC are bound to copper sites; consequently, in addition to having copper sites available for chemisorption, the composite material contains free carboxylic acid groups that are available for coordination.<sup>39</sup>

Powder X-ray diffraction was used to characterize the effect of the copper and BTC impregnation on the structure of the MCM-41 matrix. Fig. 5 compares the XRD spectra of the base MCM-41 material, the copper impregnated MCM-41, and the

composite material. A high degree of MCM-41 structural ordering is indicated by the four discrete sharp peaks in the low angle spectrum for all three samples.<sup>40</sup> The decrease in intensity of peaks in the spectrum of the composite material can be attributed to scattering by the BTC.<sup>41–43</sup> The  $d_{100}$  peak is shifted to a lower angle and broadened slightly in the spectrum of the composite material. This shift represents an expansion of the MCM-41 lattice after incorporation of BTC into the pores of the Cu-MCM-41, as has been shown previously.<sup>44</sup>

XRD scans in the higher  $2\theta$  range were also performed to characterize the structure of the composite material. As shown in Fig. 6, the XRD spectrum of the composite exhibits peaks representing a crystalline material similar to that of the CuBTC crystals. The peaks present in the composite scan have lower intensities than those of CuBTC. Some of the peaks in the higher  $2\theta$  region are eclipsed by background noise. The peaks of the composite scan that correspond to CuBTC peaks are a result of the formation of CuBTC impurities formed during synthesis of the composite material. Because there is a small concentration of CuBTC within the amorphous BTC-impregnated composite, the CuBTC peaks are of lower intensity, but still visible, on the long range XRD scan. The composite spectrum also shows a broad MCM-41 peak located between  $20$  and  $30^\circ$ . Coupled with the SEM information, which depicts the formation of CuBTC impurities within the composite, XRD shows that there are some CuBTC crystals formed from only a small mass fraction of the material. However, this CuBTC formation is not representative of the entire material and is an impurity.

Mixtures of CuBTC and 10 mol % Cu-MCM-41 were analyzed *via* XRD to estimate the amount of CuBTC impurity present in the composite material following the procedure of Kontoyannis and Vagenas.<sup>45</sup> For all standards, the ratio of the peak intensities at  $2.8$  and  $9.9^\circ$   $2\theta$  was examined, which correspond to the MCM-41 100 peak and a CuBTC peak. The ratio of three standards were plotted *versus* the weight percentage of one

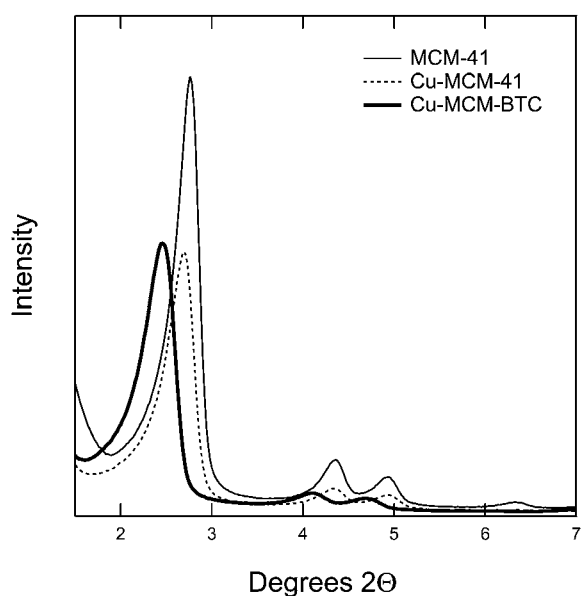


**Fig. 5** Small angle XRD scans of MCM-41, Cu-MCM-41, and Cu-MCM-BTC.

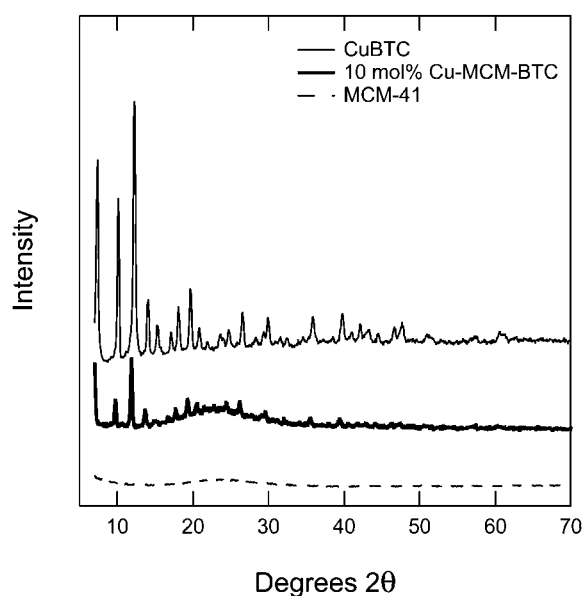


**Fig. 6** Powder XRD results for MCM-41, CuBTC, and the Cu-MCM-BTC composite. Curves are offset.

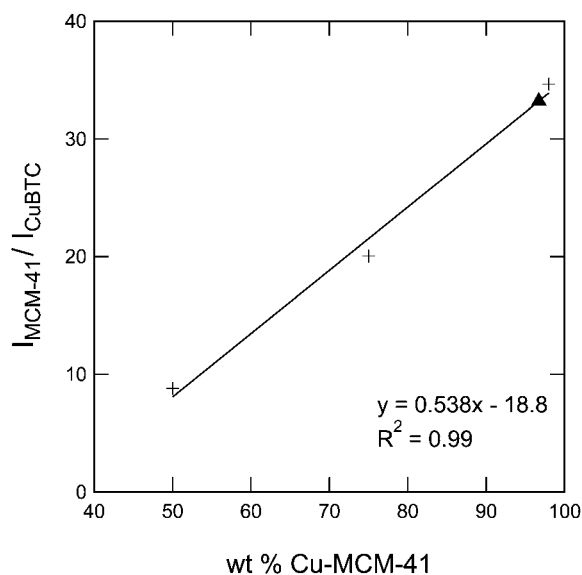


**Fig. 7** Ratio of XRD peak intensities for mixtures of CuBTC and 10 mol % Cu-MCM-41.

compound in the mixture, as seen in Fig. 7. In the resulting equation of best fit,

$$y = 0.538x - 18.8 \quad (2)$$

the parameter  $y$  represents the ratio of the peak intensities and  $x$  is the weight percentage of Cu-MCM-41 present in the mixture. From this calibration curve, the composite material was determined to have 3.3 wt % CuBTC impurity.

XPS was used to investigate the bonding of the organic phase in the composite material. Copper has been shown to fully disperse throughout the silica matrix using an impregnation technique similar to the one used in this research.<sup>46</sup> High resolution XPS scans were used to investigate the bonds occurring between the well dispersed copper sites and BTC. Fig. 8 shows

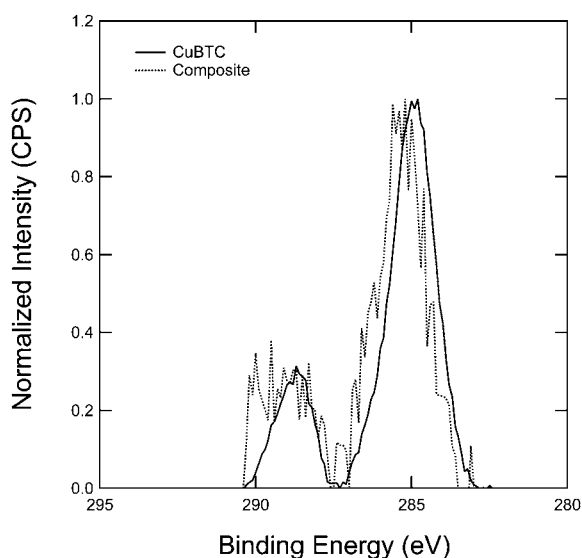


**Fig. 8** High resolution XPS spectra in the carbon region for CuBTC and the composite.

high resolution XPS scans in the carbon region, which show that carbon exists in two forms in CuBTC. The peak at 284.7 eV represents carbons in the benzene ring of BTC, and the separate 1s peak at 289.3 eV represents carbons in the carboxylic acid groups of BTC.<sup>35</sup> Analysis of the carbon region in the composite's spectrum shows a similar occurrence of the two peaks. Since all carbon atoms in the composite material are derived from the BTC and the carbon peaks in the spectra of both materials occur at the same binding energies, it is evident that the BTC molecule remains intact after synthesis of the composite. High resolution scans of the copper peaks in both samples also yield peaks that occur at the same binding energies as shown in Fig. 9. From this, we can conclude that copper in the composite material is bound to oxygen atoms from BTC in a similar way to the complexation of copper that occurs in CuBTC. However, according to the XRD and TGA results, the Cu to BTC ratio in the composite is different from that in the CuBTC. Consequently, except for BTC in the 3 wt % CuBTC impurity, the BTC molecules are bound to copper sites distributed throughout the ordered silica phase.

### 3.2 Hydrothermal conditioning

From the SEM images in Fig. 10, it is clear that the Cu-MCM-BTC sample did not change its morphology after conditioning, whereas the CuBTC degraded from octahedral crystals with sharp edges to irregularly-shaped masses. The change in morphology of CuBTC indicates that the pore structure collapsed during conditioning. There are no visible differences between SEM images for the composite material and the MCM-41 base material before and after conditioning.

This explanation can be verified using X-ray diffraction, profiles, which are shown in Fig. 11. In the XRD patterns for CuBTC, the spectrum of the conditioned material shows a decrease in peak intensity and a slight shift in the larger peaks when compared to the spectrum of virgin CuBTC. Coupled with

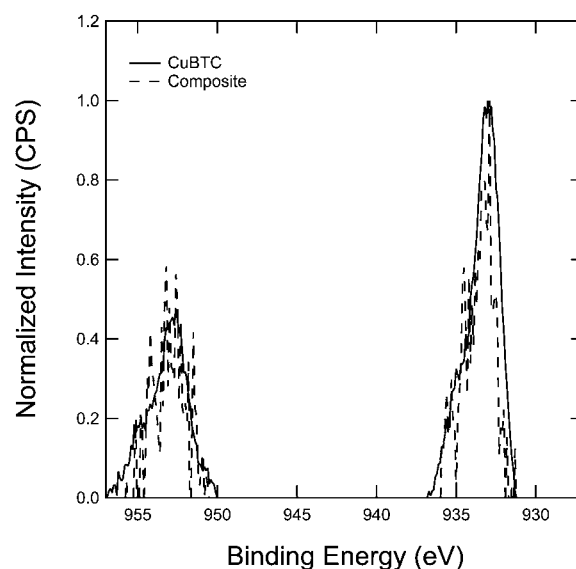


**Fig. 9** High resolution XPS spectra in the copper region for CuBTC and the composite.

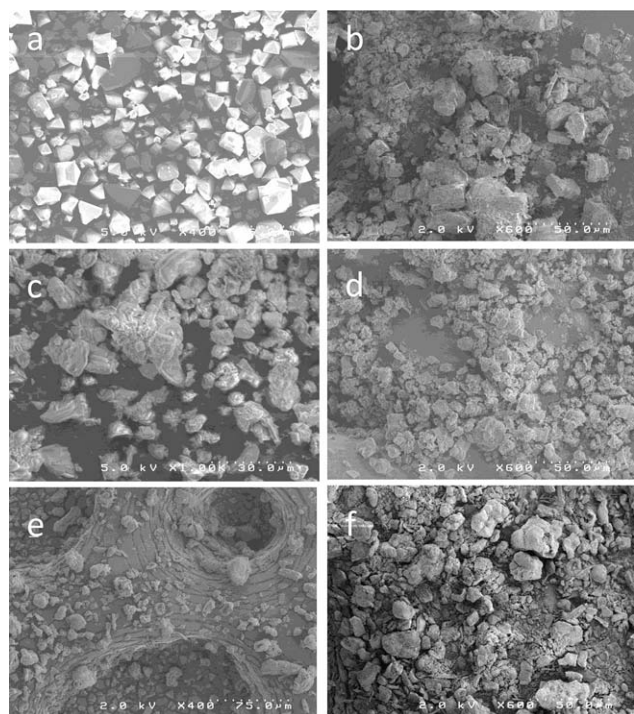


**Fig. 10** SEM images of the samples before and after conditioning for 5 h for (a) CuBTC, (b) conditioned CuBTC, (c) MCM-41, (d) conditioned MCM-41, (e) Cu-MCM-BTC, (f) conditioned Cu-MCM-BTC.

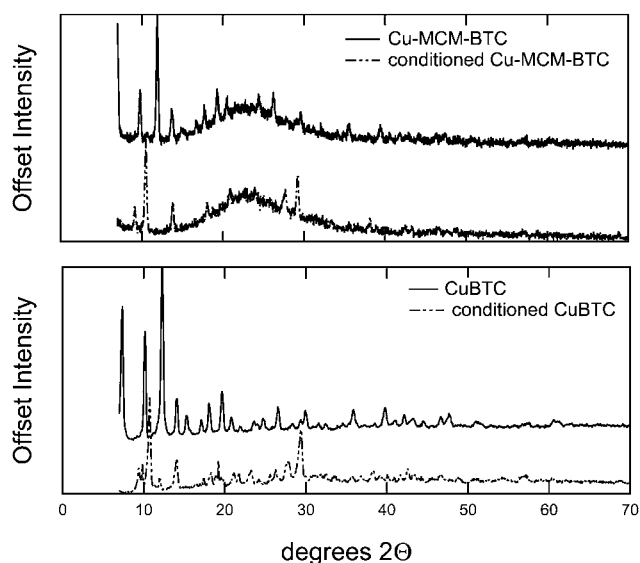


**Fig. 11** Comparison of XRD spectra before and after conditioning for CuBTC and Cu-MCM-BTC. Curves are offset.

the SEM images, the shift in the spectrum and its degradation is indicative of decomposition of the CuBTC structure. The conditioned Cu-MCM-BTC spectrum is similar to that of the conditioned CuBTC, suggesting that the small amount of CuBTC impurity located within the Cu-MCM-BTC composite material degraded during the conditioning procedure.

The small angle X-ray diffraction spectra of the conditioned Cu-MCM-BTC composite and conditioned MCM-41 samples,

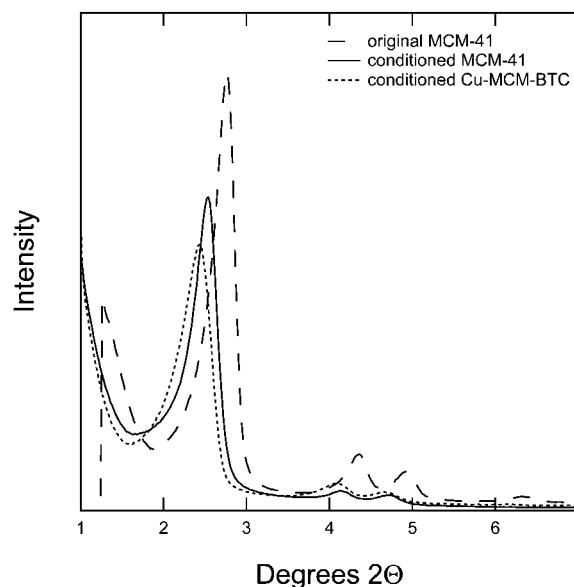


**Fig. 12** Small angle XRD spectra of MCM-41 before and after conditioning and Cu-MCM-BTC after conditioning.

shown in Fig. 12, indicate that both the composite and the base MCM-41 materials do not lose their hexagonal MCM-41 order during the conditioning process. Consequently, the powder XRD profiles show that the composite remains structurally ordered after conditioning, similar to the base MCM-41 material.

High resolution XPS spectra of the carbon atoms in the conditioned sample confirm the presence of BTC after conditioning. The same carbon peaks are present in the composite spectrum before and after conditioning. The peaks at 284 and 289 eV represent carbons in the benzene ring and the carboxylic acid groups of the organic molecule. The presence of these peaks in the spectrum indicates that BTC remains intact after conditioning.

### 3.3 Ammonia adsorption

The Cu-MCM-BTC composite is a novel adsorbent material with a high ammonia capacity, as shown in Table 2. The ammonia capacities measured using the breakthrough apparatus have standard deviations on the order of 3%. The initial ammonia capacity for the composite is 61% higher than that of MCM-41 and 46% lower than that of CuBTC. The adsorbents show a step-wise increase in ammonia capacity upon addition of the BTC impregnant within the MCM-41. Base MCM-41 begins with an ammonia capacity of 2.0 mol kg<sup>-1</sup> and increases to

**Table 2** Ammonia capacities before and after conditioning for MCM-41, CuBTC, and Cu-MCM-BTC

Sample	Ammonia Capacity (mol kg <sup>-1</sup> )	
	Initial	Conditioned
CuBTC	9.6	1.5
MCM-41	2.0	3.4
Cu-MCM-BTC	5.2	4.3

5.2 mol kg<sup>-1</sup> after functionalization with copper and BTC. The ammonia capacity of the composite material is approximately 30 times that of a common commercial carbon, BPL activated carbon (0.16 mol kg<sup>-1</sup>) and more than three times that of a common zeolite, 13X molecular sieve (1.5 mol kg<sup>-1</sup>), under the same breakthrough test conditions.

As shown in the table, the ammonia capacity of the base MCM-41 increased 41% after conditioning. As part of its synthesis procedure, MCM-41 is calcined at a high temperature to remove excess surfactant from its pores. This calcination process also strips the silica matrix of hydroxyl groups on the walls of the MCM-41. The conditioning process allows hydroxyl groups to re-form at these sites and remain after the sample is regenerated.<sup>24</sup> These additional hydroxyl groups increase the acidity of the MCM-41, which results in an increase in ammonia capacity for the conditioned sample. Consequently, the base MCM-41 shows an increase in ammonia capacity after conditioning, which is believed to be caused by the extra hydroxyl groups formed on the silica matrix during the hydrothermal treatment.

Despite having a lower ammonia capacity than CuBTC, after conditioning in saturated water vapor for 5 h the composite material maintains its structural stability and shows an ammonia capacity decrease of only 17%. Comparatively, the ammonia capacity of the CuBTC sample decreased 84% upon conditioning. The enhanced stability of the composite material, when compared to CuBTC, is due to the presence of the silica matrix. The degradation of the crystalline CuBTC impurity in the composite material upon conditioning is partially responsible for the observed decrease in ammonia capacity. The composite did lose ammonia capacity after steam conditioning. We can assume that the CuBTC impurity in the composite has the same decrease in the ammonia capacity after conditioning as the pure CuBTC MOF. If we treat the metal-organic phase and MCM-41 separately and assume that the MCM-41 in our composite has the same ammonia capacity as the pure MCM-41 after conditioning, a material balance calculation shows that the ammonia capacity for the metal-organic phase decreased about 30% after conditioning. However, if we treat the metal-organic phase and MCM-41 as an entity and assume that the MCM-41 does not behave in the composite exactly as it does by itself because of more limited access to its surface, then the material balance indicates that the composite loses only 13% of its ammonia capacity after conditioning. This result, coupled with the XRD results, indicates that the composite has a higher stability compared to CuBTC, which lost about 84% of its ammonia capacity after conditioning due to the loss of its porosity<sup>13</sup> and collapse of its structure.

The composite material has four types of active sites available for ammonia adsorption. First, the base silica matrix provides ammonia capacity.<sup>18,19,46</sup> Second, the addition of hydroxyl groups to the silica surface from exposure to humid air, steam, or liquid water enhances the ammonia capacity; the composite is synthesized using a liquid solvent of water and ethanol, and all materials are steamed for hydrothermal conditioning. Third, the copper sites distributed throughout the matrix provide additional sites for ammonia to form diammine-copper complexes.<sup>27,46</sup> Finally, carboxylic acid groups on the organic molecule provide coordination sites for the ammonia.<sup>25,47</sup>

The retention of the structure of the composite material and minimal decrease in ammonia capacity after conditioning are indicative of hydrothermal stability. In contrast, the degradation of the CuBTC structure and decrease in ammonia capacity upon conditioning is indicative of low hydrothermal stability.

## 4 Conclusions

A new composite material has been synthesized and characterized by combining an ordered mesoporous silica phase, specifically MCM-41 impregnated with copper and benzene-1,3,5-tricarboxylic acid, the organic BTC linker used in the synthesis of a common MOF, to give an ordered mesoporous silica-metal organic (MSMO) composite material. The nitrogen isotherm confirms the formation of the mesoporous composite material. According to TGA results, approximately 12% organic BTC is loaded onto the MCM-41 and bound to the copper sites dispersed throughout MCM-41. X-ray diffraction results confirm that the composite does not lose its long range MCM-41 order after impregnation with the BTC. It also confirms that small amounts of CuBTC crystals (about 3 wt %) are present in the final sample as an impurity. SEM images confirm this observation. XPS shows that copper sites that are distributed throughout the MCM-41 matrix are actively bound to BTC. The presence of both copper sites and intact BTC result in an ammonia capacity that is higher than the base ordered mesoporous silica (5.2 mol kg<sup>-1</sup> compared to 2.0 mol kg<sup>-1</sup>) due to the functionality provided by the metal organic phase.

After hydrothermal conditioning, the novel composite material maintains its high ammonia capacity, whereas the corresponding metal organic framework sample degrades, resulting in a large decrease in ammonia capacity. XPS shows that the BTC present in the composite material remains intact after conditioning. XRD shows that the MCM-41 structure is also maintained. These results show that the new composite material provides both the high ammonia capacity associated with MOF materials and the hydrothermal stability associated with the silica phase, and is a promising candidate for ammonia removal applications.

## 5 Acknowledgements

We are grateful to the U.S. Army Edgewood Chemical and Biological Center for the support of this research.

## References

- 1 V. Ravat, D. B. Mantri, P. Selvam and P. Aghalayam, *J. Mol. Catal. A: Chem.*, 2009, **314**, 49–54.
- 2 C. Chanquia, K. Sapag, E. Rodriguez-Castellon, E. Herrero and G. Eimer, *J. Phys. Chem. C*, 2010, **114**, 1481–1490.
- 3 D. Lensveld, J. Mesu, A. van Dillen and K. de Jong, *Microporous Mesoporous Mater.*, 2001, **44–45**, 401–407.
- 4 R. Savidha and A. Pandurangan, *Appl. Catal., A*, 2004, **262**, 1–11.
- 5 D. A. Sheppard and C. E. Buckley, *Int. J. Hydrogen Energy*, 2008, **33**, 1688–1692.
- 6 A. Vinu, K. Nandhini, V. Murugesan, W. Bohlmann, V. Umamaheswarl, A. Poppl and M. Hartmann, *Appl. Catal., A*, 2004, **265**, 1–10.
- 7 C. Wu, Q. Gao, J. Hu, Z. Chen and W. Shi, *Microporous Mesoporous Mater.*, 2009, **117**, 165–169.
- 8 A. Gervasini, C. Messi, P. Carniti, A. Ponti, N. Ravasio and F. Zaccheria, *J. Catal.*, 2009, **262**, 224–234.



- 9 D. Britt, H. Furukawa, B. Wang, T. G. Glover and O. M. Yaghi, *Proc. Natl. Acad. Sci. U. S. A.*, 2009, **106**, 20637–20640.
- 10 N. L. Rosi, J. Eckert, M. Eddaoudi, D. T. Vodak, J. Kim, M. O’Keeffe and O. M. Yaghi, *Science*, 2003, **300**, 1127–1129.
- 11 D. Britt, D. Tranchemontagne and O. M. Yaghi, *Proc. Natl. Acad. Sci. U. S. A.*, 2008, **105**, 11623–11627.
- 12 J. J. Low, A. I. Benin, P. Jakubczak, J. F. Abrahamian, S. A. Faheem and R. R. Willis, *J. Am. Chem. Soc.*, 2009, **131**, 15834–15842.
- 13 J. Liu, Y. Wang, A. I. Benin, P. Jakubczak, R. R. Willis and M. D. LeVan, *Langmuir*, 2010, **26**, 14301–14307.
- 14 L. Grajciar, O. Bludsky and P. Nachtigall, *J. Phys. Chem. Lett.*, 2010, **1**, 3354–3359.
- 15 P. Kussgens, M. Rose, I. Senkovska, H. Frode, A. Henschel, S. Siegle and S. Kaskel, *Microporous Mesoporous Mater.*, 2009, **120**, 325–330.
- 16 C. T. Kresge, M. E. Leonowicz, W. J. Roth, J. C. Vartuli and J. S. Beck, *Nature*, 1992, **359**, 710–712.
- 17 F. Hoffmann, M. Cornelius, J. Morell and M. Froba, *Angew. Chem., Int. Ed.*, 2006, **45**, 3216–3251.
- 18 B. A. Morrow and I. A. Cody, *J. Phys. Chem.*, 1976, **80**, 1998–2004.
- 19 B. A. Morrow, I. A. Cody and L. S. M. Lee, *J. Phys. Chem.*, 1975, **79**, 2405–2408.
- 20 N. Chino and T. Okubo, *Microporous Mesoporous Mater.*, 2005, **87**, 15–22.
- 21 T. G. Glover, K. I. Dunne, R. J. Davis and M. D. LeVan, *Microporous Mesoporous Mater.*, 2008, **111**, 1–11.
- 22 J. M. Kim, J. H. Kwak, S. Jun and R. Ryoo, *J. Phys. Chem.*, 1995, **99**, 16742–16747.
- 23 S. Shen and S. Kawi, *Langmuir*, 2002, **18**, 4720–4728.
- 24 T. Linssen, K. Cassiers, P. Cool and E. F. Vansant, *Adv. Colloid Interface Sci.*, 2003, **103**, 121–147.
- 25 C. Petit and T. Bandoz, *J. Mater. Chem.*, 2009, **19**, 6521–6528.
- 26 C. Petit and T. Bandoz, *Adv. Mater.*, 2009, **21**, 4753–4757.
- 27 C. Petit and T. Bandoz, *Adv. Funct. Mater.*, 2010, **20**, 111–118.
- 28 C. Petit, B. Mendoza and T. Bandoz, *Langmuir*, 2010, **26**, 15302–15309.
- 29 S. J. Yang, J. Y. Choi, H. K. Chae, J. H. Cho, K. S. Nahm and C. R. Park, *Chem. Mater.*, 2009, **21**, 1893–1897.
- 30 B. Liu, H. Shioyama, H. Jiang, X. Zhang and Q. Xu, *Carbon*, 2010, **48**, 456–463.
- 31 G. Hundal, Y. K. Hwang and J. S. Chang, *Polyhedron*, 2009, **28**, 2450–2458.
- 32 *Toxic FAQ Sheet for Ammonia*. Agency for Toxic Substances and Disease Registry (ATSDR). September 2004.
- 33 J. Helminen, J. Helenius and E. J. Paatero, *J. Chem. Eng. Data*, 2001, **46**, 391–399.
- 34 C. J. Doonan, D. J. Tranchemontagne, T. G. Glover, J. R. Hunt and O. M. Yaghi, *Nat. Chem.*, 2010, **2**, 235–238.
- 35 J. F. Moulder, W. F. Stickle, P. E. Sobol, K. D. Bomben, *Handbook of X-ray Photoelectron Spectroscopy: A Reference of Standard Spectra for Identification and Interpretation of XPS Data*, Chigasaki City, Japan, 2007.
- 36 R. Ryoo and S. Jun, *J. Phys. Chem. B*, 1997, **101**, 317–320.
- 37 K. A. Cychosz and A. J. Matzger, *Langmuir*, 2010, **26**, 17198–17202.
- 38 D. R. Lide, W. M. Haynes, *CRC Handbook of Chemistry and Physics*, CRC Press, Boca Raton, FL, 2009.
- 39 B. Mu, F. Li and K. S. Walton, *Chem. Commun.*, 2009, 2493–2495.
- 40 D. Trong On, S. M. J. Zaidi and S. Kaliaguine, *Microporous Mesoporous Mater.*, 1998, **22**, 211–224.
- 41 B. Marler, U. Oberhagemann, S. Vortmann and H. Gies, *Microporous Mater.*, 1996, **6**, 375–383.
- 42 S. Syukri, C. Fischer, A. Al Hmaideen, Y. Li, Y. Zheng and F. Kuhn, *Microporous Mesoporous Mater.*, 2008, **113**, 171–177.
- 43 J. Goworek, A. Kierys, W. Gac, A. Borowka and R. Kusak, *J. Therm. Anal. Calorim.*, 2009, **96**, 375–382.
- 44 S. Damyanova, L. Dimitrov, R. Mariscal, J. L. G. Fierro, L. Petrov and I. Sobrados, *Appl. Catal., A*, 2003, **256**, 183–197.
- 45 C. G. Kontoyannis and N. V. Vagenas, *Analyst*, 2000, **125**, 251–255.
- 46 A. M. B. Furtado, Y. Wang, T. G. Glover and M. D. LeVan, *Microporous Mesoporous Mater.*, 2011, DOI: 10.1016/j.micromeso.2011.01.027.
- 47 M. Seredych, A. B. Tamashauskyy and T. J. Bandoz, *Adv. Funct. Mater.*, 2010, **20**, 1670–1679.